Defect Detection and Depth Estimation in CFRP through Phase of Transient Response of Flash Thermography

***Abstract*—This paper presents a new method called phase of transient response using the local reference pixel vector (PTR-LRPV) to process pulsed thermography data for defect detection and depth estimation in carbon fiber reinforced polymer specimens. Due to the use of flash as excitation source in pulsed thermography and subsequently its adaptation with the conditions of suddenly applied input, the received signal from the infrared camera can be separated into two transient and steady-state responses in the frequency domain. Defects cause local variations in the thermal spatio-temporal patterns that the transient response can fairly reveal such highly informative variations. On the other hand, the steady-state response mainly includes the intrinsic characteristics of the specimen (sound areas). In fact, by properly separating these responses and employing the phase of the transient term, a suitable distinction of defect characteristics from sound areas has been reached. The results show that the proposed PTR-LRPV is effective in both defect detection and depth estimation tasks, and also, can fairly compete with several well-known algorithms in terms of both quantitative and qualitative criteria.**

***Index Terms*—Carbon fiber reinforced polymers (CFRP), pulsed thermography, non-destructive testing (NDT), phase of transient response, suddenly applied input.**

I. Introduction

CARBON fiber reinforced polymers (CFRP) are composite materials that have properties such as high corrosion resistance, high strength-to-weight ratio, flexibility in large-scale complex designs and proper stability under various environmental conditions [1]. These have led to many industrial applications, such as aerospace [2], automotive [3], wind turbine blades [4], transportation and infrastructure [5]. Due to their non-ideal manufacturing procedure or exposure to stressful environments during use, CFRPs are prone to defects, which cause to reduce their performance and structural integrity. Therefore, non-destructive testing (NDT) techniques are essential to monitor the CFRPs' quality [6]. In this regard, various NDT techniques such as X-ray [7], ultrasound [8], terahertz waves [9] and infrared thermography [10] are mainly used to detect defects in CFRPs.

In pulsed thermography, which is from the infrared thermography category, heat excitation is applied to the specimen using an optical flash (a very short duration thermal pulse, about some milliseconds). After applying the excitation, the thermal energy is partially absorbed by the CFRP surface and converted to heat, which then diffuses through the specimen. However, internal defects restrict this heat diffusion that leads to an increase in temperature in such areas and provokes some thermal patterns on the specimen surface. These patterns are captured by an infrared (IR) camera as a time sequence of thermograms. Thanks to its acceptable accuracy in the quick and non-contact inspection of vast areas and also easy automation capability, pulsed thermography (PT) has achieved significant acceptance in recent years in dealing with various types of defects, such as flat bottom holes (FBH), Inserts and barely visible impact damage (BVID) [11], [12].

However, there are some difficulties in this field: empirical nature of NDT methods, inevitable presence of noise, non-uniform thermal excitation, and lateral heat diffusion. Moreover, flash thermography itself is suffered from the highly diffusive and strongly damped nature of the excited thermal waves, which causes the proper detection of small and deep defects to be very challenging [11]. Hence, various signal processing algorithms have been suggested to deal with these challenges in thermography data. These processes try to enhance the distinction between defects and sound areas and as such lead to more accurate defect detection. The most well-known algorithms in this field are thermographic signal reconstruction (TSR) [13], principal component thermography (PCT) [14], and pulsed phase thermography (PPT) [15]. In the TSR, fitting the raw data (obtained from the IR camera) to the low-order logarithmic polynomials leads to noise reduction and also contrast enhancement between defect and sound areas [13]. PCT is based on the singular value decomposition (SVD) in which 3D data is first converted into a 2D matrix (by allocating the thermal sequences as the rows of a huge 2D matrix) and then decomposed onto the empirical orthogonal functions (EOF) for feature extraction purpose. The results indicate that only the first few EOFs are sufficient to appropriately display defects [14]. The PPT method analyzes thermal data in the frequency domain using the discrete Fourier transform (DFT). Since the phase response is more robust to non-uniform heating, emissivity variations, and environmental noise, it has more capability for detecting deeper defects in comparison with raw data and amplitude response [16]. Further, some new approaches have been reported recently; in [17] a hybrid spatial and temporal

segmentation methodology is introduced which fuses features in multiple dimensions. This scheme also consists of a Sequence-PCA layer in the learning process which leads to extra semantic information. Authors in [18] have proposed a structured iterative alternating sparse matrix decomposition framework, which allows the abnormal patterns to be extracted automatically for flaw contrast enhancement. In [19], some deep learning-based methods have been reported for defect detection. Besides, to take advantage of different techniques, several hybrid methods have also been proposed in this field [20]- [24]. In [20], a combination of neural networks and principal component analysis (PCA) is used to estimate the depth of the defect. In another method, the PCA-based dimension reduction followed by the independent component analysis (ICA) is employed to detect defects [21]. In [22], using the optical flow, the motion properties of the thermal patterns are extracted and then applied to the PCA algorithm, which leads to convenient results in microcrack detection. In [23], differential absolute contrast (DAC) and TSR techniques are used to reduce the noise of thermal images, and then the K-Means clustering is utilized to classify the statistical features extracted from the IR images. Also, in [24], based on the physics characteristics of the defect in inductive thermograph, a defect segmentation method is proposed. The segmentation threshold is determined based on the first-order statistical properties and then optimized using the genetic algorithm.

Most of the existing thermographic researches only focused on defects detection, but a more challenging task is to estimate the depth of defects which is crucial for many applications. Various depth estimation methods have been reported in the literature. In [25], the concept of peak slope time is employed to estimate the depth. Authors in [26] used the nonlinear transfer model of peak contrast time analysis to reach a reliable depth estimation. Several defect depth estimation methods employed learning-based methodologies such as artificial neural networks [20], [27]. However, due to their training stage, such systems are highly dependent on basic information about the type and depth of defects. Also, the main challenge arises when it needs to examine datasets with different properties. In fact, the inconsistency between training and testing data can significantly reduce the performance of learning-based methods. Some other depth estimation methods have been introduced based on frequency domain analysis. In several works, the inverse relationship between defect depth and blind frequency has been used to estimate depth [11], [28] and [29]. Besides, inspired by [30], some methods developed based on a direct relationship between the depth of defect and phase [31], [32]. In [11], a new approach, called adaptive spectral band integration, is introduced, in which, the phase contrast is integrated over the relevant frequency range in a pixel-wise manner, resulting to a unique index map for defect.

Several depth estimation methods have also been introduced based on other thermography techniques such as eddy current pulsed thermography [33]-[35], and vibrothermography [36], [37]. In [33], time analysis is performed to select optimal time windows for kernel-PCA. Then the depth evaluation in these time windows is done using the norm of the principal components and derivatives of the impulse response. In [34], the crossing point of impulse responses related to defective and sound areas, and also, the skewness of impulse responses are used for the depth estimation. In [35], a modified skewness calculation through inverting heating response has been proposed. This modified skewness feature removed the counteracting effect of the temperature distribution in the heating and cooling stages, which led to a highly sensitive and linear model for depth estimation. In [36], depth estimation is done based on ~~the~~ three features in the temperature-time curve: half-maximum power time, peak slope time, and the second derivative peak time. The model showed a relationship between the defect's depth and these features. In [37], a low-power vibrothermography scheme is introduced based on the pulse compression approach. An analytical relation of the lag of the compressed pulse versus the delamination depth was presented, showing a straightforward way to perform depth inversion in vibrothermographic testing. ~~the peak extraction, time delay, and compressed phase pulse, which provides a lag quantity that is suitable for depth estimation.~~

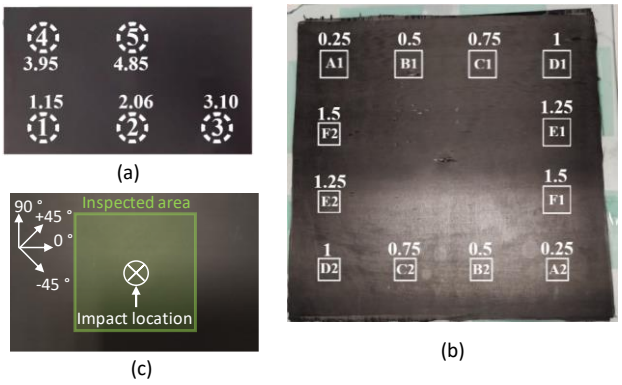

Fig. 1. Three investigated CFRP specimens with (a) flat-bottom holes, (b) Inserts and (c) barely visible impact damage.

The common thermography signal processing techniques try to emphasis those spatio-temporal variations of the thermal sequences that lead to better discrimination between defect and sound areas. In the case of deeper defects, insufficient energy received from the excitation source results in poor variations in the thermal patterns, which causes these defects to behave similar to sound areas. Thus, it is more challenging to highlight variations of the thermal patterns in such cases. Generally speaking, the existing methods have some issues in dealing with very deep defects. With particular attention to the nature of the signal received from the IR camera, this work attempts to highlight weak thermal patterns. The profile of the received signal depends on various conditions such as environment, IR camera characteristics, excitation source, and the specimen's material, among which this article focuses on the excitation source. Due to the consistency of pulsed thermography with the suddenly applied input conditions, the received signal from the IR camera is divided into two transient and steady-state responses [38]. But since there is no proper distinction between the responses in the time domain, this work has focused on their DFT to achieve proper separation. Thus, a new methodology based on the phase of transient response called *phase of*

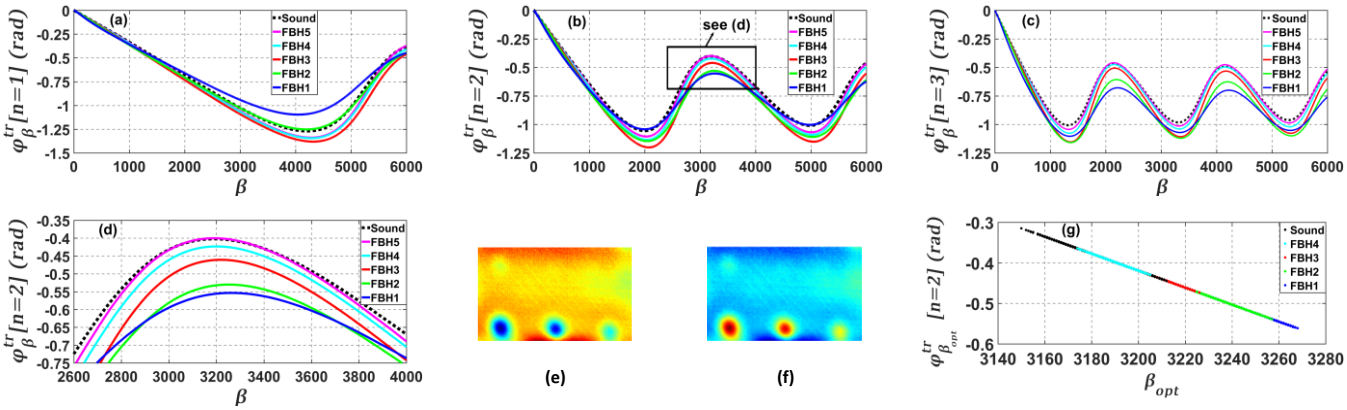

Fig. 2. Comparison of the transient response phase ($\varphi_\beta^{tr}[n]$) as a function of β for a sample of the sound area and a sample of each defect with (a) $n = 1$, (b) $n = 2$, and (c) $n = 3$, (d) magnified version of the peak occurred in (b) for β in the range of [2600: 4000]. Also, the images obtained using the peak of $\varphi_\beta^{tr}[n = 2]$, and using β_{opt} are shown in parts (e) and (f), respectively. Further, (g) shows the relation between $\varphi_{\beta_{opt}}^{tr}[n = 2]$ and β_{opt} for all pixels.

transient response using the local reference pixel vector (PTR-LRPV) is presented. The experimental results showed that this new technique is promising for defect detection and depth estimation for both categories of shallow and deep defects.

The paper is organized as follows: In Section II, test specimens and experimental setup are briefly described. Section III focuses on how to carefully separate between the transient and steady-state responses in such a way that be useful for defect detection and depth estimation purposes. After that, the validation of the proposed method and its comparison with some well-known algorithms are presented in Section IV, and finally, Section V concludes the paper.

II. Material and Experimental Setup

The experiments are performed on three autoclave manufactured CFRP specimens: the first one ($CFRP_{FBH}$) which is shown in Fig. 1(a) has a $150 \times 90 \times 5.5$ mm^3 plate with layup $[(-45/0/45/90)_3]_s$ and includes five circular flat-bottom holes (FBH) with the same diameter of 10 mm. For simplicity, in the rest of this paper, these defects are named as FBH1, FBH2, FBH3, FBH4, and FBH5, which have diameter to depth ratios of 8.69, 4.85, 3.22, 2.53, and 2.06, respectively. The remaining material thicknesses of this defects (in mm) are illustrated in Fig. 1(a). The second specimen, ($CFRP_{INSERT}$) which is shown in Fig. 1(b), is a CFRP laminate with dimensions $300 \times 300 \times 3$ mm^3 with layup $[(0/90)_3]_s$ which was manufactured using resin transfer molding. During manufacturing, various Insert defects are introduced. These defects are made from double folded Brass foil which are sealed with flash-breaker tape. The Inserts A1, B1, C1, D1, E1, and F1 have a size of 20×20 mm^2 and length-to-depth ratio of 80.00, 40.00, 26.66, 20.00, 16.00 and 13.33, respectively. The Inserts A2, B2, C2, D2, E2, and F2 have a size of 15×15 mm^2 and length-to-depth ratios of 60.00, 30.00, 20.00, 15.00, 12.00 and 10.00, respectively. Their depth (in mm) are depicted in Fig. 1(b). The third specimen, shown in Fig. 1(c), is a CFRP coupon with size of $140 \times 90 \times 5.5$ mm^3, and quasi-isotropic layup of $[(+45/0/-45/90)_3]_s$. The specimen was impacted by dropping a 7.72 kg impactor from a height of 0.3 m (measured impact energy of 18.5 J) using a calibrated drop tower, introducing barely visible impact damage (BVID).

All experiments are performed in reflection mode, which means that the excitation source (flash) and IR camera are on the same side. To ensure that sufficient energy is transmitted to the entire surface of the specimen, it is fixed at about 70 cm away from the source. The type of the IR camera is FLIR A6750sc, which has following properties: a) cryo-cooled InSb detector with a pixel density of 640×512 pixels, b) noise equivalent temperature difference (NETD) of < 20 mK, and c) bit depth of 14 bit. An internal infrared filter is employed, which narrows the camera's spectral range from 1– 5 µm to 3– 5 µm. The flash excitation arises from a Hensel linear flash lamp with a nominal energy of 6 kJ and time duration of 5 milliseconds. The experiments are performed at room temperature for $CFRP_{FBH}$, $CFRP_{INSERT}$ and $CFRP_{BVID}$ specimens, using a recording time of 120, 60 and 50 seconds, and also, a framerate of 50, 30 and 50 Hz, respectively. The excitation lamp has been located in such a way to avoid its direct reflection into the lens of the camera and also to have a heat distribution as uniform as possible over the specimen's surface.

III. Methodology

A. Suddenly Applied Input

Assuming that the received signal by the IR camera in the time domain, t, is represented as $T(t)$ and given the discrete-time variable as $t_k = k\Delta t$ such that Δt is the sampling time step, and $k = 0, 1, 2, ..., N-1$, the received signal can be expressed in discrete form as $T[k\Delta t] \equiv T[k]$. Also, assuming a linear time invariant (LTI) system with input $I[k]$, impulse response $h[k]$, and output $T[k]$, therefore $T[k] = I[k] * h[k]$, where * indicates the convolution operator. Because of using a short-duration high-intensity pulse (an overdamped flash) to excite the specimen under investigation, the input can be properly approximated as $I[k] = \delta[k]$ which expresses suddenly applied behavior. Thus, the output is the same as impulse response ($T[k] = \delta[k] * h[k] = h[k]$), consequently, due to the adaptation of the pulse thermography to the suddenly applied

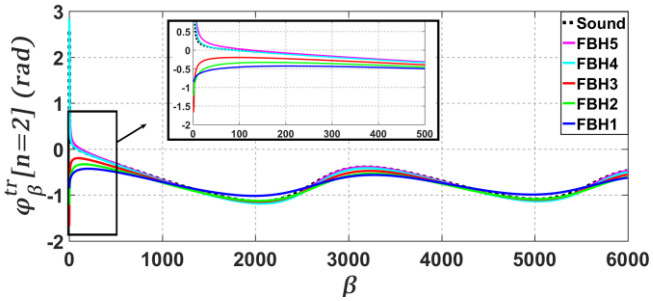

Fig. 3. Comparison of the $\varphi_\beta^{tr}[n=2]$ curves for β in the range of [0: N-1] using $T_{ref}[k\Delta t]$ for the defects' centers and a sample sound area. Also, a magnified version of the beginning part (for β in the range of [0: 500]) is illustrated.

input conditions, the signal received by the IR camera can be separated into two parts as follows [38]:

$$T[k] = T^{tr}[k] + T^{ss}[k] \quad (1)$$

where $T^{tr}[k]$ and $T^{ss}[k]$ are the transient and steady-state impulse responses, respectively. $T^{tr}[k]$ is mostly manifested by the suddenly applied input's characteristics, which means its effect disappears fairly quickly. In contrast, $T^{ss}[k]$ mainly refers to the characteristics of the system itself. It provides the intrinsic features of the system, which means its effect is long-lasting. Further, the defect's effects appear after flash excitation as local variations in the thermal spatio-temporal patterns, and then, disappear with the complete cooling of the specimen. Therefore, the defect property can be associated with $T^{tr}[k]$. Sound areas reflect the characteristics of the specimen itself. Obviously, the effect of these areas is present even after the effect of the defects has disappeared. Hence, the sound areas property can be associated with $T^{ss}[k]$. Thus, it seems that the proper separation between $T^{tr}[k]$ and $T^{ss}[k]$ can lead to a reliable defect detection result.

B. *Transient Response*

The goal of this section is to efficiently separate between $T^{tr}[k]$ and $T^{ss}[k]$ for the IR camera's received signal ($T[k]$). Given (1), $T^{tr}[k]$ can be expressed as:

$$T^{tr}[k] = T[k] - T^{ss}[k]. \quad (2)$$

Since (2) cannot be easily separated in the time domain, the calculations have been transferred to the frequency domain using DFT. Assuming that the received signal by the IR camera in the frequency domain, f, is represented as $F(f)$ and given the discrete-frequency variable as $f_n = n/N\Delta t$ where $n = 0,1,2,\dots,N-1$, the received signal can be expressed in discrete form as $F[n/N\Delta t] \equiv F[n]$, which is the DFT of the $T[k]$ and can be written as follow

$$F[n] = \Delta t \sum_{k=0}^{N-1}\left(T[k\Delta t]e^{(-2\pi ink/N)}\right) = Re[n] + i\, Im[n] \quad (3)$$

where N is the total number of the captured thermograms from the IR camera, i is the imaginary number, $Re[n]$ and $Im[n]$ are respectively the real and imaginary parts of the $F[n]$. According to (2), property of the suddenly applied input, and utilizing DFT, it can be shown that in the frequency domain [38]

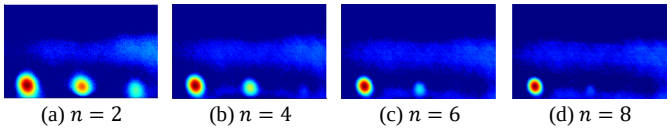

(a) $n = 2$ (b) $n = 4$ (c) $n = 6$ (d) $n = 8$

Fig. 4. Output images obtained from β_{opt} at $\varphi_\beta^{tr}[n]$ using $T_{ref}[k\Delta t]$ for the frequencies corresponding to (a) $n = 2$, (b) $n = 4$, (c) $n = 6$ and (d) $n = 8$.

$$F_\beta^{tr}[n] = F[n] - F_\beta^{ss}[n] = \Delta t \sum_{k=0}^{N-1}\left(T[k\Delta t]e^{(-2\pi ink/N)}\right) - \Delta t \sum_{k=\beta}^{N-1}\left(T[k\Delta t]e^{(-2\pi ink/N)}\right) = Re^{tr}[n] + i\, Im^{tr}[n] \quad (4)$$

where, $F_\beta^{tr}[n]$ is the DFT of the $T^{tr}[k]$, $F_\beta^{ss}[n]$ is the DFT of the $T^{ss}[k]$, $Re^{tr}[n]$ and $Im^{tr}[n]$ are respectively the real and imaginary parts of the $F_\beta^{tr}[n]$ and also β is the threshold level for separating the total and steady-state responses, which can be defined in $[0,1,\dots,N-1]$ interval. Here to calculate $F_\beta^{tr}[n]$ in (4), by choosing an optimum β value (which is named β_{opt} hereafter), $F_\beta^{ss}[n]$ is firstly computed and then subtracted from $F[n]$. $F_\beta^{ss}[n]$ is the DFT of $T[k]$ over a finite interval $[\beta, N-1]$, in which $T[k]$ mainly contains the steady-state response' characteristics. Determining β_{opt} in such a way that leads to a reliable separation between $F_\beta^{ss}[n]$ and $F_\beta^{tr}[n]$ is challenging, and this task will be studied in Section III.C.

In the frequency domain, the processes can be done on both amplitude and phase. Given that the phase response shows better ability for defect detection in thermography [16], this work employs phase response. The phase of transient response (PTR) can be written as below

$$\varphi_\beta^{tr}[n] = \tan^{-1}(Im^{tr}[n]/Re^{tr}[n]). \quad (5)$$

C. *Processing Using the Phase of Transient Response (PTR)*

This section aims to find β_{opt}, for proper separation of the steady-state response from the total response, which consequently results in a reasonable $\varphi_\beta^{tr}[n]$. According to (4) for each pixel, $F_\beta^{tr}[n]$ is calculated from its time history in the thermal sequence for different values of β, and then by using (5), $\varphi_\beta^{tr}[n]$ can be determined. Also, based on the value of n, the evaluations are performed on a particular frequency, which is determined by $f_n = n/N\Delta t$. Fig. 2(a)-(c) show $\varphi_\beta^{tr}[n]$ as a function of β for those frequencies corresponding to respectively $n = 1, 2,$ and 3, in the time sequence of pixels from the centers of each defect and a pixel in a sound area. As can be understood, the total number of peaks and valleys is $2n$. In fact, the $exp^{-2\pi ink/N}$ in (4), passes n periods with length of 2π for $k = [0, N-1]$. Additionally, in Fig. 2 (a)-(c), despite the relative similar behavior of $\varphi_\beta^{tr}[n]$ curves in defective and sound areas, there are significant distinctions in their peaks. For instance, a peak of the Fig. 2(b) is emphasized in Fig. 2(d), for $\beta = [2600: 4000]$. As can be seen in Fig. 2(d), there is an appropriate contrast between the defect and sound areas, as well as between the different types of defects in terms of depth. In fact, for the shallowest defect (FHB1), the curve of the $\varphi_\beta^{tr}[n = 2]$

is further away from the curve of the sound area (indicated by black). As a result, it can be stated that β_{opt} for an appropriate separating between transient and steady-state responses is the same β that peaks up the $\varphi_{\beta}^{tr}[n]$.

Fig. 2(e), shows the corresponding image of $\varphi_{\beta}^{tr}[n=2]$. This image is obtained as follows: for each pixel, firstly $\varphi_{\beta}^{tr}[n=2]$ is calculated for $\beta = [2600:4000]$ (the range of the peaks for the pixels), and then the maximum of $\varphi_{\beta}^{tr}[n=2]$ is chosen ($\varphi_{\beta_{opt}}^{tr}[n=2]$). In this figure, the FBHs 1, 2, and 3 are well distinguished from the sound areas and are clearly identifiable, but the FBH4 is hard to identify, and the FBH5 is not visible at all. Further, for each pixel, the β_{opt} is employed and the result is demonstrated in Fig. 2(f). In this figure, the distinction between the defect and sound areas is very similar to that of Fig. 2(e) except that the intensity levels of the defects relative to the sound areas are in contrast to Fig. 2(e). As shown in Fig. 2(g), there is a linear relation with a negative slope between them, thus, the concept of the images in Fig. 2 (e) and (f) is the same. To simplify the proposed method in this paper, the strategy that is used in Fig. 2(f) is employed.

D. PTR Using the Reference Pixel Vector (PTR-RPV)

As mentioned in previous subsections (III.B and III.C), in (4), for a given pixel, firstly, choosing the β_{opt} the $F_{\beta}^{ss}[n]$ has to be calculated, and then by subtracting this term from $F[n]$, the $F_{\beta}^{tr}[n]$ can be obtained. Also, $F_{\beta}^{tr}[n]$ is mainly related to the defects' features, while $F_{\beta}^{ss}[n]$ is mainly related to the sound areas' features. Hence, instead of using the time sequence vector for each pixel to determine $F_{\beta}^{ss}[n]$, a single common vector as a reference for all pixels can be used. One reasonable suggestion for creating this reference vector is to use the time sequence of sound areas. Therefore, in this case, $F_{\beta}^{tr}[n]$ can be obtained as follows

$$F_{\beta}^{tr}[n] = \Delta t \sum_{k=0}^{N-1}\left(T[k\Delta t]exp^{(-2\pi ink/N)}\right) - \Delta t \sum_{k=\beta}^{N-1}\left(T_{ref}[k\Delta t]exp^{(-2\pi ink/N)}\right) \quad (6)$$

where $T_{ref}[k\Delta t]$ is the reference pixel vector (RPV) that must be chosen from the sound area. However, due to the unknown location of the defects, choosing this RPV can be challenging. Thus, by calculating the median value for each thermogram in the time sequence for the 3D IR data, a vector of these medians is achieved that can be a proper candidate for $T_{ref}[k\Delta t]$. The motivation for using the median operator is that the defect area is mainly smaller than the sound ones in thermograms, thus this operator can give a good approximation for the time sequence of the sound area. In Fig. 3, $\varphi_{\beta}^{tr}[n=2]$ are shown as a function of $\beta = [0: N-1]$, for the central pixels of the defects and also a pixel in the sound area, which are obtained by first using (6) to determine $F_{\beta}^{tr}[n]$, and then utilizing (5) to determine $\varphi_{\beta}^{tr}[n]$. Due to using a fixed vector for all pixels with sound areas' characteristics, it is expected that β_{opt} occurs in the range of [0 500], which consequently leads to a proper separation between defects and sound areas. It also can be seen in Fig. 3, for relatively low-depth defects (FBH1 to FBH3), $\varphi_{\beta}^{tr}[n=2]$ starts from some negative values, then increase drastically and finally after reaching its peaks, demonstrate gradually decreasing behaviors. However, for sound areas, $\varphi_{\beta}^{tr}[n=2]$ starts at a positive value and drastically decreases. Notice, due to the more depth in comparison to others, FBH4 and FBH5 behave like a sound area.

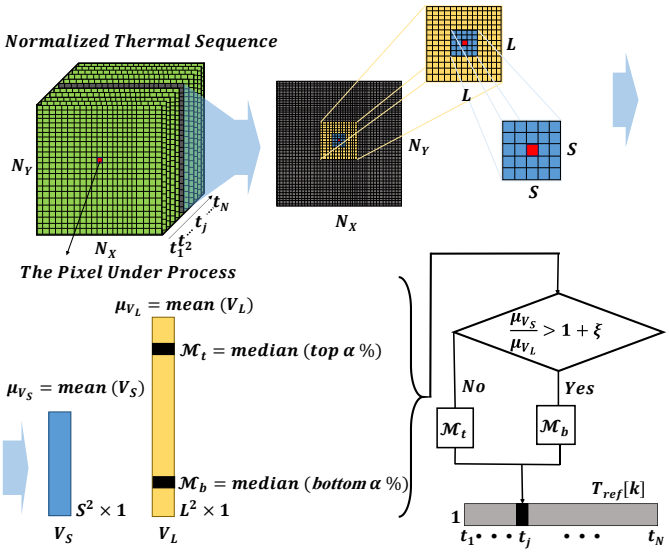

Fig. 5. Schematic of how to obtain $T_{ref}[k\Delta t]$ for each pixel in the proposed PTR-LPRV method.

In this regard, in Fig. 4, for every pixel in its thermal sequence, the values of $\varphi_{\beta}^{tr}[n]$ for $\beta = [0: 500]$ are calculated using (5 and 6), and then the β_{opt} is chosen. Fig. 4(a-d) are obtained at frequencies corresponding to $n = 2, 4, 6$ and 8, respectively. In Fig. 4(a), the FBH1, 2 and 3 are well recognizable. Also, FBH1 and 2 in Fig. 4(b), and only the FBH1 in Fig. 4(c and d), are clearly detected. However, deeper defects FBH4 and 5 are not detectable here. Overall, this method shows good quality in the case of low to mid-depth defects, but in the deeper cases, the quality is lost.

E. PTR Using the Local Reference Pixel Vector (PTR-LRPV)

In Section III.D, the vector $T_{ref}[k\Delta t]$ was calculated from the median of each thermogram in the time sequence, and this vector was utilized in the calculation of $F_{\beta}^{ss}[n]$ for all pixels. This section will consider a local windowing strategy to determine an adaptive $T_{ref}[k\Delta t]$ for each thermogram. This can be promising because; although the various areas of the specimen are usually exposed by slightly non-uniform radiation from the excitation source, local regions are usually affected by uniform radiations. The idea is that in each thermogram, a local window is considered around each pixel, and then $T_{ref}[k\Delta t]$ is calculated using the median of all pixels within the window during its time sequence (in the 3rd dimension of the dataset). Of course, the unideal allocation of the defective areas' pixels is a challenge in this local strategy that can negatively affect the $T_{ref}[k\Delta t]$ of such areas, which reduces the accuracy of $F_{\beta}^{ss}[n]$. To overcome this problem, a new methodology based on the

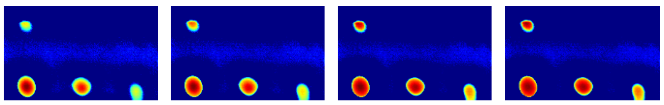

(a) $\alpha = 50\%$ (b) $\alpha = 30\%$ (c) $\alpha = 10\%$ (d) $\alpha = 5\%$

Fig. 6. Output images of the proposed PRT-LRPV method for the frequency corresponding to $n = 2$, with (a) $\alpha = 50\%$, (b) $\alpha = 30\%$, (c) $\alpha = 10\%$, and (d) $\alpha = 5\%$.

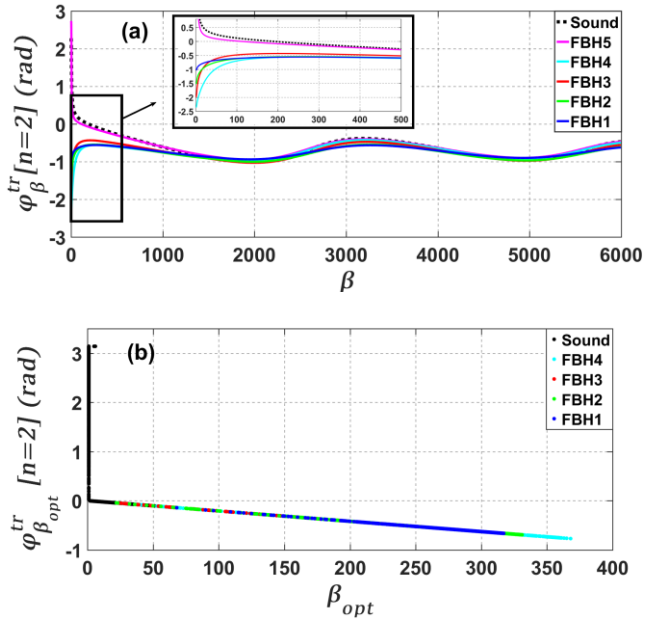

Fig. 7. (a) Comparison of the $\varphi_\beta^{tr}[n = 2]$ curves for β in the range of $[0: N - 1]$ in the proposed PRT-LRPV method for the defects' centers and a sample sound area. Also, a magnified version of the beginning part of (a), for β in the range of $[0: 500]$ is illustrated. (b) $\varphi_{\beta_{opt}}^{tr}[n = 2]$ as a function of β_{opt} for all pixels.

use of a more advanced windowing procedure is presented, which is schematically presented in Fig. 5. The main idea is quite simple: defective areas have a higher temperature in comparison to their neighbors. The procedure is as follows: firstly, the whole thermal data is normalized into the [0 1] interval and then, for each pixel in the thermograms, a large $L \times L$ window and also a small $S \times S$ window are chosen. Next, in the thermogram under investigation (jth thermogram), these small and large windows firstly unfold to two vectors, which are called V_S^j and V_L^j respectively and afterwards the mean of them are calculated and named $\mu_{V_S}^j$ and $\mu_{V_L}^j$, respectively.

Then, for better estimation of $T_{ref}[k\Delta t]$, the following inequality with a constant parameter ξ is used to eliminate such areas which potentially belong to defective areas from the calculation of $T_{ref}[k\Delta t]$:

$$\mu_{V_S}/\mu_{V_L} > 1 + \xi. \tag{7}$$

If this condition is met, there is a high possibility that the pixel under investigation belongs to the defective area. In fact, in such areas, high temperatures result in some high mean values as well. Therefore, this condition can provide a proper insight about the sound areas to determine $T_{ref}[k\Delta t]$. Also V_L^j is sorted in a descending manner and the median of the top α-percent and the bottom α-percent of this vector are calculated and named $\mathcal{M}_t^j$ and $\mathcal{M}_b^j$, respectively. For defective area, the bottom of vector V_L^j, due to the lower temperature values, is a good candidate for surrounding sound areas of the defect, thus, the $\mathcal{M}_b^j$ can be selected as the jth element of $T_{ref}[k\Delta t]$. On the other hand, if (7) does not hold, there is a high possibility of the pixel belongs to the sound area, that in such situations, the $\mathcal{M}_t^j$ can be selected as the jth element of $T_{ref}[k\Delta t]$. By repeating this procedure for all thermograms, the vector $T_{ref}[k\Delta t]$ can be determined for the pixel under processing. Then, $\varphi_\beta^{tr}[n]$ is calculated using (6) and then (5), and finally the β_{opt} can be subsequently determined. Hereafter, this method is called the *phase of transient response using the local reference pixel vector* (PTR-LRPV).

The constant parameter ξ depends on the thermal data specifications and corresponding processing parameters. To achieve an optimal value, a relation is set based on the following reasonable assumptions:

1) Assume μ_{tot} be the mean of the entire normalized thermal data, thus, by increasing μ_{tot}, it can be stated that the ratio of μ_{V_S}/μ_{V_L} in (7) will also be increased, which results $\xi \propto \mu_{tot}$.
2) Let the size of L be fixed; by increasing the size of S, two windows become closer together, which consequently gets closer μ_{V_S} and μ_{V_L} as well. Therefore, in this condition, a smaller ξ is needed for proper separation of the defect and sound areas, thus $\xi \propto 1/S$.
3) Assume a fixed size for S, by increasing the size of L, the windows diverge further from each other. This can lead to more different mean values as well, and subsequently this implies the need for a bigger ξ, thus $\xi \propto L$.

Based on the abovementioned issues, the parameter ξ is empirically obtained as below,

$$\xi = C_1 \mu_{tot} \sqrt{L/S}. \tag{8}$$

where C_1 is a constant and empirically set to 1.50. Based on many experiments and by considering the signal to noise (SNR) ratio and a reasonable computational cost, the windows sizes are determined as $L = 51$ and $S = 17$.

To determine the value of α, the images obtained from the PTR-LRPV are shown in Fig. 6, where the FBHs 1 to 4 are detected well for different values of α. As can be seen, a lower α values lead to a higher contrast for output images that motivate us to use $\alpha = 5$ hereafter (notice the high contrast of the deep FBH4). However, very deep FBH5 could even not be detected by this method. In Fig. 7(a) the curves of $\varphi_\beta^{tr}[n = 2]$ for $\beta = [0: N - 1]$ are shown by the PTR-LRPV method. As can be seen in this figure, the curves of the FBHs 1 to 4 are well-separated from the curve of the sound area, especially, notice to the behavior of FBH4, which formerly in Fig. 3, was quite similar to the sound areas, and now, the PTR-LPV approach detects it very well via highlighting this defect's poor thermal sequence variations. In Fig. 7(b), $\varphi_{\beta_{opt}}^{tr}[n = 2]$ is illustrated for all pixels as a function of β_{opt}. It can be seen that except for

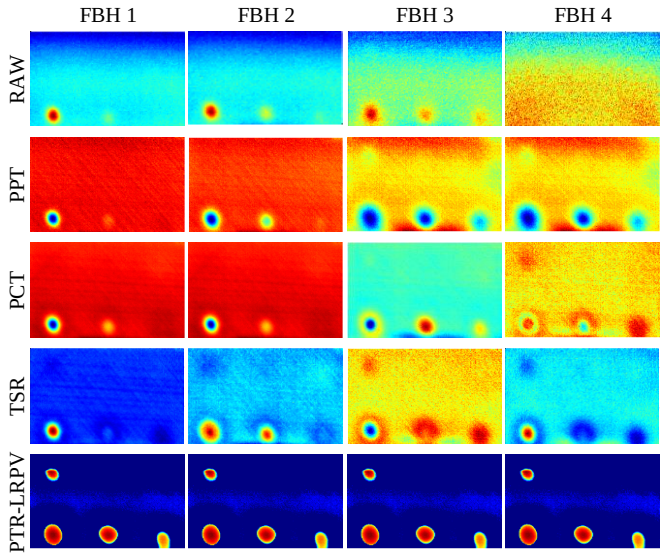

Fig. 8. Output results of the different processing methods for the $CFRP_{FBH}$.

$\beta_{opt} = 0$, belonging to the sound area, there is a linear relation with a negative slope between $\varphi^{tr}_{\beta_{opt}}[n = 2]$ and β_{opt}, which is similar to Fig. 2(g). In most pixels of sound areas, despite the different $\varphi^{tr}_{\beta_{opt}}[n = 2]$ values, the $\beta_{opt} = 0$, resulting in fairly smooth sound areas. Since the PTR-LRPV method uses β_{opt} instead of $\varphi^{tr}_{\beta_{opt}}[n]$, it offers this smoothness, leading to the high contrast between the defect and sound areas.

F. *Depth estimation*

This section focuses on estimating the depth of the defect. To this, the classical equation in the frequency domain, using in PPT method is considered, and then, it will be modified with the PTR-LPV. The depth of the defect is inversely proportional to the square root of the blind frequency [11], [28] and [29]:

$$z = C_2\sqrt{\alpha/\pi f_b} \tag{9}$$

where z is the defect depth, α is the thermal diffusivity of the specimen under investigation, $b \in 0,1,2,\dots,N-1$, and $f_b = b/N\Delta t$ is the blind frequency, i.e. the frequency at which the defect has no contrast compared to the sound areas. $C_2 \in [1.5\ 2]$ is an empirical constant for phase transform and usually set to 1.82. Based on what is mentioned in [30] and according to Fig. 7(a), the phase values at $\beta = 0$ for different defects have a direct relation with their depths (i.e. $z \propto \varphi$, where φ is the phase). Our experimental results confirm a direct but monotonic relationship between the defect depth and transient response phase. Therefore, inspired by (9) and by using the transient response phase, the following equation is suggested to estimate the defect depth:

$$z = C_3\sqrt{\alpha\,|\bar{\varphi}^{tr}_0|/\pi\, f_b} \tag{10}$$

where C_3 is a constant parameter, fixing to 1.45, and $\bar{\varphi}^{tr}_0$ is expressed as:

TABLE I
SNR (DB) RESULTS OF THE PROPOSED PRT-LRPV COMPARED TO SEVERAL WELL-KNOWN SIGNAL PROCESSING METHODS FOR THE $CFRP_{FBH}$. THE BEST RESULTS ARE SHOWN IN BOLDFACE.

FBHs	Raw	PPT	PCT	TSR	PRT-LRPV
FBH1	29.18	61.98	54.64	63.68	**68.53**
FBH2	14.61	47.15	43.89	43.29	**66.24**
FBH3	10.83	27.06	27.90	31.51	**55.15**
FBH4	–	2.78	15.34	13.93	**54.11**

TABLE II
DEFECT DEPTH ESTIMATION RESULTS USING PPT (9) AND PTR-LRPV (10) METHODS FOR THE $CFRP_{FBH}$. IN EACH ROW, THE CLOSEST ESTIMATE TO THE ACTUAL DEPTH VALUE IS SHOWN IN BOLDFACE.

FBHs	Actual depth	PPT	PTR-LRPV
FBH1	1.15	1.26	**1.15**
FBH2	2.06	**2.02**	**2.10**
FBH3	3.10	2.68	**3.13**
FBH4	3.95	3.10	**3.99**

$$\bar{\varphi}^{tr}_0 = \frac{1}{N_d}\sum \varphi^{tr}_0\Big|_{\max(\Delta\varphi)} \tag{11}$$

in the above equation, φ^{tr}_0 is the transient response phase at $\beta = 0$ and N_d is the total number of the defective area's pixels. Since the defective area usually consists of more than one pixel, therefore, in (11), the value of $\bar{\varphi}^{tr}_0$ is determined by averaging the φ^{tr}_0 values of those pixels which are detected as the defective area pixels by the proposed PTR-LRPV approach. In addition, max(Δφ) expression means that φ^{tr}_0 is determined at the frequency that leads to the highest phase contrast between the defect and sound areas, which is the same as frequency that led to proper defect detection.

IV. *DISCUSSION AND COMPARATIVE STUDIES*

In this section, the proposed PRT-LRPV method is compared with raw data as well as with some well-known thermography processing methods, such as TSR [13], PCT [14], and PPT [15]. For numerical assessments, the signal-to-noise ratio (SNR) index is used, which is defined in dB as follows

$$SNR = 20\,log_{10}\left|\left(\mu_{R_d} - \mu_{R_S}\right)/\sigma_{R_s}\right| \tag{12}$$

μ_{R_d} is the mean of pixels in the defect area, μ_{R_S} and σ_{R_s} are the mean and standard deviation of the pixels in the sound area, and it is assumed that the sound area is the whole specimen except the defective regions.

A. *Comparative Study– $CFRP_{FBH}$*

The results for $CFRP_{FBH}$ are shown in Fig. 8. In all cases, the best possible result of each method is provided. Table I provides a comparison of the SNR values obtained for four defects of $CFRP_{FBH}$ specimen by different algorithms. Fig. 8 and Table I show that for all four defects, the PRT-LRPV method offers good results and yields the highest SNR. More notably, in the case of the deep defect FBH4, it does not appear in the raw data

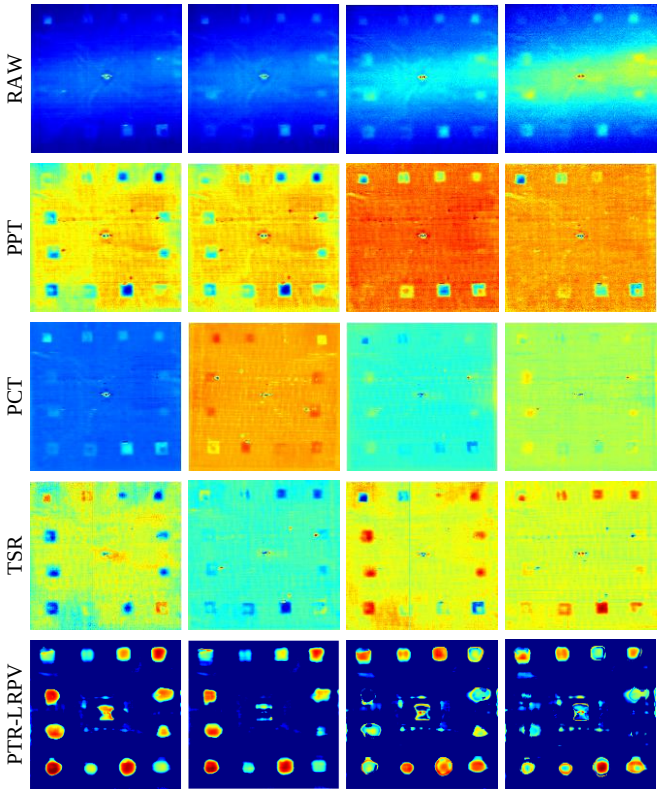

Fig. 9. Output results of the different processing methods for the $CFRP_{INSERT}$.

and even is not detectable in the comparative methods or is poorly detected. Thus, this defect is considered very challenging, and provides a good indication of the performance of the different methods. As can be seen, our proposed PRT-LRPV method gives a fairly high contrast output image (high qualitative performance) for it and also has an $SNR = 54.40$ dB (high quantitative performance). The very deep defect FBH5 could not be detected by any of the methods, not even by our proposed PRT-LRPV approach. Considering that FBH5 is a circular defect with diameter 10 mm, and located at a depth of 4.85 mm in a CFRP sample having high in-plane thermal diffusion, this might not come as a surprise. Table II presents the defect depth estimation results for $CFRP_{FBH}$ specimen using the PPT (9) and PTR-LRPV (10) methods. Both methods have yielded acceptable results for shallow defects (FBHs 1 and 2). However, the advantage of the proposed method over the classical one is more evident in the case of deep defects (FBHs 3 and 4). For these deep defects, the accuracy of the PPT method has significantly decreased, but the proposed PTR-LRPV still yields reliable estimates of the defect depth.

B. Comparative study – $CFRP_{INSERT}$

Fig. 9 shows the results of the different methods for $CFRP_{INSERT}$ specimen. Table III also gives the SNR values. Most defects in raw data are difficult to detect or not detectable at all. However, different processing methods, in some cases, provide good results and show good defect detection performance. In the proposed PRT-LRPV method, almost all

TABLE III
SNR (DB) RESULTS OF THE PROPOSED PRT-LRPV FOR THE $CFRP_{INSERT}$ SPECIMEN COMPARED TO SEVERAL WELL-KNOWN SIGNAL PROCESSING METHODS. THE BEST RESULTS ARE SHOWN IN BOLDFACE.

Inserts	Raw	PPT	PCT	TSR	PRT-LRPV
A1	2.56	31.71	24.91	26.26	**33.67**
B1	1.24	26.18	12.93	27.44	**32.96**
C1	0.86	27.02	13.76	27.57	**35.23**
D1	–	29.19	20.25	25.22	**35.91**
E1	–	7.18	13.24	11.25	**32.44**
F1	–	3.82	9.99	14.57	**22.48**
A2	3.45	42.17	34.78	41.61	**42.71**
B2	3.65	**47.81**	41.75	45.43	46.83
C2	2.61	28.58	14.01	31.45	**37.29**
D2	–	32.74	23.39	34.12	**47.04**
E2	–	22.71	24.87	26.89	**43.37**
F2	–	24.45	27.59	33.51	**43.28**

TABLE IV
DEFECT DEPTH ESTIMATION RESULTS USING PPT AND PTR-LRPV METHODS FOR THE $CFRP_{INSERT}$. IN EACH ROW, THE CLOSEST ESTIMATE TO THE ACTUAL DEPTH VALUE IS SHOWN IN BOLDFACE

Inserts	Actual depth	PPT	PTR-LRPV
A1	0.25	0.34	**0.25**
B1	0.50	0.56	**0.48**
C1	0.75	**0.79**	**0.71**
D1	1.00	**0.95**	**0.95**
E1	1.25	1.21	**1.27**
F1	1.50	1.21	**1.48**
A2	0.25	0.40	**0.26**
B2	0.50	0.61	**0.57**
C2	0.75	**0.76**	0.72
D2	1.00	1.16	**0.92**
E2	1.25	1.21	**1.26**
F2	1.50	1.42	**1.51**

defects are fairly detectable, and it offers some promising results, which is also numerically confirmed by Table III. Although for Insert B2, the PPT method has the highest SNR, this defect is simply detectable by all methods, and meanwhile, the result of PRT-LRPV is very close to the PPT's one in this case. To summarize, it can be stated that the proposed PRT-LRPV method can reasonably compete with other well-known defect detection methods. Also, the proposed method provides high contrast output images. This high contrast property can be suitable for machine vision purposes, where the good separation between defects and sound areas is very demanding. Due to the fact that the resin was injected from the middle of the plate during the resin transfer molding process. This resulted in an unintentional manufacturing defect at the injection location. But as can be seen in Fig. 9, the PRT-LRPV method was also able to detect this unintentional defect relatively well.

Table IV presents the results of defect depth estimation for the $CFRP_{INSERT}$ specimen using PPT (9) and PRT-LRPV (10). As can be seen, for both shallow (A1, A2, B1, and B2) and deep (E1, E2, F1, and F2) defects, the results of the PRT-LRPV are

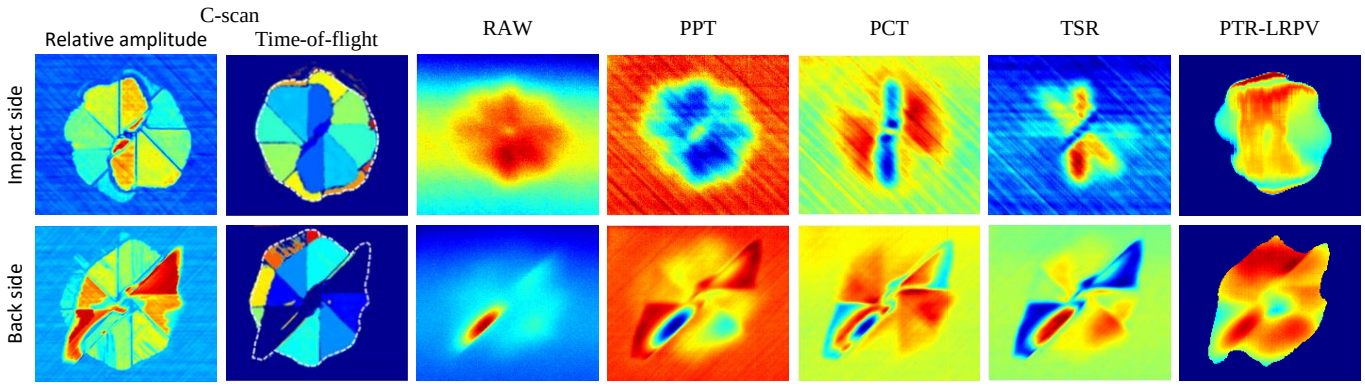

Fig. 10. Output results of the different processing methods for the $CFRP_{BVID}$.

more suitable. In the case of relatively deep defects (C1, C2, D1, and D2), the performances of the two methods are close to each other. Generally, the results of the proposed PRT-LRPV method are more accurate than the PPT ones, which indicates that this method is more reliable for estimating the depth of defects for the $CFRP_{INSERT}$ specimen.

C. *Comparative study – $CFRP_{BVID}$*

This is one of the common defect types that may take place in composites. The complex nature of BVIDs makes their proper detection quite challenging. Thus, this third specimen can consider as a major test for judging the quality of different algorithms. As a benchmark for further comparisons, the ultrasonic pulse-echo C-scans, obtaining from both impact and back sides using a 5 MHz focused transducer are shown in Fig. 10. This figure consists of the corresponding relative amplitude and time-of-flight images. To have a meaningful comparison with thermographic results, the defect borders are highlighted on the C-scan images. Also, for both sides, the output images from the raw data, PPT, PCT, TSR, and PTR-LRPV methods are shown in Fig. 10. Those images have been selected such that to provide the best indication of the defect according to the C-scan results. As can be seen, the results of the PTR-LRPV method are closer to the C-scan images, and this method can reasonably separate the defect area from the sound area.

V. Conclusions

In this paper, it has been shown that due to the nature of pulse thermography, considering the suddenly applied input condition can properly address the defect detection and depth estimation problems. In this regard, the transient response phase is separated from the intrinsic characteristics of the received signal. Accordingly, a novel method based on phase of transient response using the local reference pixel vector (PTR-LRPV) has been proposed. To evaluate its effectiveness, this algorithm has been applied on three CFRP specimens with different defect types (FBHs, Inserts, and BVID). The results showed that the proposed method is competitive with the well-known existing methods. The high contrast output images (as can be seen in Section IV) can be considered as one of the main advantages of our algorithm. Further, due to the high sensitivity of the proposed method to the poor thermal variations, it also provided acceptable results in detecting deep defects as well as estimating their depths.

References

[1] Y. He and R. Yang, "Eddy current volume heating thermography and phase analysis for imaging characterization of interface delamination in CFRP," *IEEE Transactions on Industrial Informatics*, vol. 11, no. 6, pp. 1287–1297, 2015.

[2] J. Ahmed, B. Gao and W. Woo, "Wavelet-Integrated Alternating Sparse Dictionary Matrix Decomposition in Thermal Imaging CFRP Defect Detection," *IEEE Transactions on Industrial Informatics*, vol. 15, no. 7, pp. 4033-4043, 2019.

[3] Y. He, S. Chen, D. Zhou, S. Huang and P. Wang, "Shared Excitation Based Nonlinear Ultrasound and Vibrothermography Testing for CFRP Barely Visible Impact Damage Inspection," *IEEE Transactions on Industrial Informatics*, vol. 14, no. 12, pp. 5575-5584, 2018.

[4] R. Yang, Y. He, A. Mandelis, N. Wang, X. Wu and S. Huang, "Induction Infrared Thermography and Thermal-Wave-Radar Analysis for Imaging Inspection and Diagnosis of Blade Composites," *IEEE Transactions on Industrial Informatics*, vol. 14, no. 12, pp. 5637-5647, 2018.

[5] A. Foudazi, C. Edwards, M. Ghasr and K. Donnell, "Active Microwave Thermography for Defect Detection of CFRP-Strengthened Cement-Based Materials," *IEEE Transactions on Instrumentation and Measurement*, vol. 65, no. 11, pp. 2612-2620, 2016.

[6] D. M. Tsai, I. Y. Chiang, and Y. H. Tsai, "A shift-tolerant dissimilarity measure for surface defect detection," *IEEE Transactions on Industrial Informatics*, vol. 8, no. 1, pp. 128−137, 2012.

[7] K. I. Tserpes, A. G. Stamopoulos, and S. G. Pantelakis, "A numerical methodology for simulating the mechanical behavior of CFRP laminates containing pores using X-ray computed tomography data," *Composites Part B: Engineering*, vol. 102, pp. 122−133, 2016.

[8] W. Post, M. Kersemans, I. Solodov, K. Van Den Abeele, S. García and S. van der Zwaag, "Non-destructive monitoring of delamination healing of a CFRP composite with a thermoplastic ionomer interlayer," *Composites Part A: Applied Science and Manufacturing*, vol. 101, pp. 243-253, 2017.

[9] H. Zhang et al., "Terahertz Amplitude Polynomial Principle Component Regression for Aramid–Basalt Hybrid Composite Laminate Inspection," *IEEE Transactions on Industrial Informatics*, vol. 14, no. 12, pp. 5601-5609, 2018.

[10] H. Wang, N. Wang, Z. He and Y. He, "Phase-Locked Restored Pseudo Heat Flux Thermography for Detecting Delamination Inside Carbon Fiber Reinforced Composites," *IEEE Transactions on Industrial Informatics*, vol. 15, no. 5, pp. 2938-2946, 2019.

[11] G. Poelman, S. Hedayatrasa, J. Segers, W. Van Paepegem and M. Kersemans, "Adaptive spectral band integration in flash thermography: Enhanced defect detectability and quantification in composites," *Composites Part B: Engineering*, vol. 202, p. 108305, 2020.

[12] G. Poelman, S. Hedayatrasa, J. Segers, W. Van Paepegem and M. Kersemans, "Multi-scale gapped smoothing algorithm for robust

baseline-free damage detection in optical infrared thermography," *NDT & E International*, vol. 112, p. 102247, 2020.
[13] S. Shepard, "Reconstruction and enhancement of active thermographic image sequences," *Optical Engineering*, vol. 42, no. 5, p. 1337, 2003.
[14] N. Rajic, "Principal component thermography for flaw contrast enhancement and flaw depth characterisation in composite structures," *Composite Structures*, vol. 58, no. 4, pp. 521−528, 2002.
[15] X. Maldague and S. Marinetti, "Pulse phase infrared thermography," *Journal of Applied Physics*, vol. 79, no. 5, pp. 2694–8, 1996.
[16] H. Zhang *et al*., "Optical and mechanical excitation thermography for impact response in basalt-carbon hybrid fiber-reinforced composite laminates," *IEEE Transactions on Industrial Informatics*, vol. 14, no. 2, pp. 514–522, 2018.
[17] B. Hu et al., "A Lightweight Spatial and Temporal Multi-Feature Fusion Network for Defect Detection, "*IEEE Transactions on Image Processing*, vol. 30, pp. 472-486, 2021.
[18] Liu et al., "Structured iterative alternating sparse matrix decomposition for thermal imaging diagnostic system," *Infrared Physics & Technology*, vol. 107, p. 103288, 2020.
[19] Y. He et al., "Infrared machine vision and infrared thermography with deep learning: A review," *Infrared Physics & Technology*, vol. 116, p. 103754, 2021.
[20] S. Dudzik, "Analysis of the accuracy of a neural algorithm for defect depth estimation using PCA processing from active thermography data," *Infrared Physics & Technology*, vol. 56, pp. 1−7, 2013
[21] L. Cheng, B. Gao, G. Y. Tian, W. L. Woo, and G. Berthiau, "Impact damage detection and identification using eddy current pulsed thermography through integration of PCA and ICA," *IEEE Sensors Journal*, vol. 14, no. 5, pp. 1655–1663, 2014.
[22] Y. Wang *et al*., "Thermal Pattern Contrast Diagnostic of Microcracks With Induction Thermography for Aircraft Braking Components," *IEEE Transactions on Industrial Informatics*, vol. 14, no. 12, pp. 5563–5574, 2018.
[23] X. Lu et al., "Detection of Micro Solder Balls Using Active Thermography Technology and K-Means Algorithm," *IEEE Transactions on Industrial Informatics*, vol. 14, no. 12, pp. 5620-5628, 2018.
[24] B. Gao, X. Li, W. Woo and G. Tian, "Physics-Based Image Segmentation Using First Order Statistical Properties and Genetic Algorithm for Inductive Thermography Imaging," *IEEE Transactions on Image Processing*, vol. 27, no. 5, pp. 2160-2175, 2018.
[25] Y. Wei, S. Zhang, Y. Luo, L. Ding and D. Zhang, "Accurate depth determination of defects in composite materials using pulsed thermography," *Composite Structures*, vol. 267, p. 113846, 2021.
[26] M. Wang, B. Gao, T. Wu, B. Hu and L. Liu, "Defect depth retrieval method based on nonlinear transformation for pulsed thermographic inspection", *International Journal of Thermal Sciences*, vol. 149, p. 106196, 2020.
[27] N. Saeed, H. Al Zarkani and M. Omar, "Sensitivity and Robustness of Neural Networks for Defect-Depth Estimation in CFRP Composites," *Journal of Nondestructive Evaluation*, vol. 38, no. 3, 2019.
[28] C. Ibarra-Castanedo, "Quantitative subsurface defect evaluation by pulsed phase thermography: depth retrieval with the phase," Ph.D. Thesis, Université Laval, Québec, QC, Canada, 2005.
[29] J. Peeters, C. Ibarra-Castanedo, S. Sfarra, X. Maldague, J. Dirckx and G. Steenackers, "Robust quantitative depth estimation on CFRP samples using active thermography inspection and numerical simulation updating," *NDT & E International*, vol. 87, pp. 119-123, 2017.
[30] L. Favro, and X. Han, "Thermal wave materials characterization and thermal wave imaging," *Sensing for Materials Characterization, Processing and Manufacuring, ASNT TONES*, pp. 399-415, 1998
[31] C. Ibarra-Castanedo and X. Maldague, "Pulsed phase thermography reviewed", *Quantitative InfraRed Thermography Journal*, vol. 1, no. 1, pp. 47-70, 2004.
[32] C. Ibarra-Castanedo and X. Maldague, "Pulsed phase thermography inversion procedure using normalized parameters to account for defect size variations", *Thermosense XXVII*, 2005.
[33] Q. Yi et al., "Evaluation of debonding in CFRP-epoxy adhesive single-lap joints using eddy current pulse-compression thermography," *Composites Part B: Engineering*, vol. 178, p. 107461, 2019.
[34] Q. Yi, G. Y. Tian, H. Malekmohammadi, J. Zhu, S. Laureti and M. Ricci, "New features for delamination depth evaluation in carbon fiber reinforced plastic materials using eddy current pulse-compression thermography," *NDT & E International*, vol. 102, pp. 264-273, 2019.
[35] X. Chen, G. Y. Tian, S. Ding and J. Wu, "Investigation of Skewness Feature for Evaluation of Defects Using Eddy Current Pulsed Thermography," *IEEE Sensors Journal*, vol. 19, no. 24, pp. 12118-12125, 2019.
[36] O. Obeidat, Q. Yu and X. Han, "Analytical model for depth profiling using sonic IR NDE," *NDT & E International*, vol. 100, pp. 11-19, 2018.
[37] S. Hedayatrasa, J. Segers, G. Poelman, W. Paepegem and M. Kersemans, "Vibro-Thermal Wave Radar: Application of Barker Coded Amplitude Modulation for Enhanced Low-Power Vibrothermographic Inspection of Composites," *Materials*, vol. 14, no. 9, p. 2436, 2021
[38] A. V. Oppenheim, R. W. Schafer, and J. R. Buck, Discrete-Time Signal Processing, vol. 2. Upper Saddle River, NJ, USA: Prentice-Hall, 1999.